HHS Public Access

Author manuscript

Int J Fatigue. Author manuscript; available in PMC 2020 March 01.

Published in final edited form as:

Int J Fatigue. 2019 March ; 120: 342–352. doi:10.1016/j.ijfatigue.2018.10.015.

Investigation of the mechanisms by which hot isostatic pressing improves the fatigue performance of powder bed fused Ti-6Al-4V

P. Li[a], **D.H. Warner**[a,*], **J.W. Pegues**[b], **M.D. Roach**[c], **N. Shamsaei**[b], **N. Phan**[d]

[a]School of Civil and Environmental Engineering, Cornell University, Ithaca, NY 14853, United States

[b]National Center for Additive Manufacturing Excellence (NCAME), Department of Mechanical Engineering, Auburn University, Auburn, AL 36849, United States

[c]Department of Biomedical Materials Science, University of Mississippi Medical Center, Jackson, MS 39216, United States

[d]Structures Division, Naval Air Systems Command, Patuxent River, MD 20670, United States

Abstract

Hot isostatic pressing (HIP) is often needed to obtain powder bed fused (PBF) Ti-6Al-4V parts with good fatigue performance. This manuscript attempts to clarify the mechanisms through which HIP treatment acts to improve high cycle fatigue performance. Several mechanisms are considered and examined against experimental data sets available in the literature. The results suggest that HIP may act most significantly by decreasing the fraction of the defect population that can initiate fatigue cracks, both by decreasing defect sizes below a threshold and by changing the microstructure that surrounds defects. Given the novelty of the latter conclusion, an electron backscatter diffraction microscopy study was performed for validation. The gained understanding provides initial guidance on the choice of optimum HIP soak parameters (Temperature-Pressure-Time) for the high cycle fatigue performance of PBF Ti-6Al-4V.

Keywords

Powder Bed Fusion; Selective Laser Melting; Hot Isostatic Pressing; Ti-6Al-4V; Build Defects; Microstructure; Probabilistic Model

1. Introduction

Powder Bed Fusion (PBF) is an additive manufacturing technique that utilizes directed laser or electron beam energy to selectively fuse a bed of metal powder, layer-by-layer. PBF has been particularly appealing to the aerospace and medical device industries, as it offers an economical route to produce low volumes of geometrically complex parts. As PBF

*Corresponding author: derek.warner@cornell.edu (D.H. Warner).

technology has developed, challenges of thermal stress, surface roughness and build defects have been at the forefront, particularly for load bearing applications. While significant effort has gone into improving the PBF process to overcome such challenges, current applications often rely on post processing treatments to rectify.

In fatigue critical applications, the presence of build defects that initiate fatigue cracks can significantly degrade mechanical performance [1]. In such cases, post processing treatment typically involves hot isostatic pressing (HIP) and subsequent surface machining. The HIP treatment step consists of subjecting the part to an inert gas pressure at an elevated temperature, shrinking sub-surface defects via a hydrostatic pressure [2–4]. The subsequent surface machining is performed to remove the unaffected defects at the surface as well as the inherent surface roughness associated with powder-bed processes. It is now well established that this post processing route is effective at changing the fatigue failure mode from initiation at surface and build defects to initiation at large microstructural features. Further, PBF specimens post processed in this way have fatigue performance on par with traditionally processed materials. We illustrate this in Fig. 1, showing the results of several independent but comparable high cycle fatigue studies for laser PBF Ti-6Al-4V, the material of focus for this manuscript. The fatigue data of traditionally manufactured Ti-6Al-4V from the Metallic Materials Properties Development & Standardization [5] is used as a reference, which corresponds to specimens with a gage diameter of ~ 5 mm machined from a 25 mm thick solution treated and aged plate (1 h solution treat at ~ 926 °C, 3 h age at ~ 538 °C).

The benefits of HIP treatment are not free. HIP treatment significantly coarsens the α laths in PBF Ti-6Al-4V, as shown throughout the literature and in the micrographs presented in this paper. As specific examples, Wycisk et al. [6] showed that HIP treatment results in a coarsening of α lath thickness from < 1 μm to approximately 4 μm in laser PBF Ti-6Al-4V subjected to HIP treatment, and Seifi et al. [7] reported a doubling of the α lath width in electron beam PBF. Such microstructural coarsening is thought to be detrimental to high cycle fatigue performance and other properties [8–12]. For laser PBF Ti-6Al-4V, Leuders et al. [13] has specifically shown that HIP treatment at 1050 °C is inferior to 920 °C, and attributed this result to greater microstructural coarsening occurring in the 1050 °C case. Similar observations have been made in other materials, e.g. laser PBF AlSi12Mg [14]. This has motivated HIP treatments at higher pressures and lower temperatures together with rapid cooling [15] to limit microstructural coarsening. However, the extent to which these strategies can be pushed, while still neutralizing fatigue governing defects, needs to be established.

To optimize the HIP treatment of PBF parts, an understanding of the controlling mechanisms is key. While an appreciable number of studies have been performed to examine effects of HIP on the fatigue behavior of PBF Ti-6Al-4V [12, 13, 16, 17, 19], limited clarity has emerged regarding the mechanism, i.e. how does HIP improve high cycle fatigue performance? Accordingly, published studies involving HIP treatments of laser PBF Ti-6Al-4V have largely followed traditional guidelines: not less than 100 MPa within the range 895 to 955 °C under inert atmosphere; hold at the selected temperature within ± 15°C for 180 ± 60 min, and cool under inert atmosphere to below 425 °C [3].

This manuscript is aimed at clarifying the underlying mechanisms by which HIP treatment improves the high cycle fatigue behavior of PBF Ti-6Al-4V. It begins in section 2 by examining several plausible mechanisms considering data published in the open literature. The analysis points to a decrease in the population of defects above a critical size and suggests that consequential changes in the microstructure surrounding defects are the key mechanisms through which HIP treatment acts to improve high cycle fatigue performance. The novelty of the latter mechanism motivated a confirming electron backscatter diffraction (EBSD) microscopy study, which is discussed in section 3. Finally, the implications of the results are examined in section 4, where optimum HIP treatment parameters are discussed and modeled. Interestingly, while microstructure in the neighborhood of defects is found to be of primary importance to the effectiveness of HIP treatment, HIP process modeling must still involve the evolution of defect size, as this controls microstructural evolution.

Focus is directed towards the laser PBF process, but electron beam PBF results are referenced when additional insight is offered. With that said, we suspected much of the analysis to be relevant to electron beam PBF material, with the recommended HIP parameters for laser PBF being a conservative bound for the electron beam PBF case. In all cases, the manuscript is focused on specimens that have undergone a surface treatment step after HIP, e.g. machining. The fatigue performance of as-built PBF specimens manufactured with current technology is governed by defects at or near the surface of the specimen [1]. These defects are not generally neutralized by HIP and heat treatments [2, 20]; and thus, a surface treatment post-processing step is necessary for good high cycle fatigue performance (Fig. 1). In other words, the scope of the manuscript is limited to specimens governed by fatigue crack initiation from interior defects, i.e. surface treated specimens subjected to high cycle fatigue loading.

2. Why is hot isostatic pressing (HIP) effective?

Studies to date have indicated that heat treatment alone offers negligible improvement of laser PBF Ti-6Al-4V fatigue performance [1, 12, 13], except perhaps in cases where the relief of residual stresses is important [11, 21]. Defect populations have been shown to change substantially under HIP treatment (but not heat treatment) [12] and are the observed source of the life limiting fatigue cracks in surface treated specimens [21–24]. Microstructure evolution during HIP treatment is not expected to be substantially influenced by the ≤1 GPa hydrostatic pressure [25], consistent with the similar appearance of SEM micrographs [12] and EBSD phase maps [13] comparing HIP and heat treated specimens that experienced the same thermal history. Thus, with respect to high cycle fatigue performance, the effectiveness of HIP treatment can be attributed to its action on the potential fatigue crack initiating defects.

2.1. Elimination of defects

HIP treatment is often reported to eliminate sub-surface defects, both in laser PBF Ti-6Al-4V [6, 11, 26, 27] and electron beam PBF Ti-6Al-4V [7, 28, 29]. However, closer inspections suggest that this is not the case. With high resolution X-ray computed tomography (CT) (4 μm)[1], Kasperovich et al. [12] detected a sub-surface defect volume

fraction of 0.012 % after HIP of laser PBF Ti-6Al-4V, where the as-built defect volume fraction was 0.077 %. Similarly, starting with an even greater as-built sub-surface defect volume fraction, Leuders et al. [32] found a ~ 0.112 % defect volume fraction after HIP, with defect sizes up to ~ 86 μm.

Several works point to an increasing internal pressure of insoluble argon gas within defects, as the reason that defects in laser PBF Ti-6Al-4V do not fully close during HIP treatment [33]. The argon gas can originate not only from the laser PBF build chamber, but also from the gas atomization process used to create Ti-6Al-4V powder. The role of the latter is apparent when considering HIP treatment of electron beam PBF Ti-6Al-4V parts built in vacuum. Both Cunningham et al. [34] and Tammas-Williams et al. [35] observed the regrowth of gas pores during heat treatment following HIP of electron beam PBF Ti-6Al-4V, but no regrowth of lack of fusion defects which do not have an internal argon pressure [34].

Given the above, it appears incorrect to assert that the removal of defects is the mechanism by which HIP treatment improves high cycle fatigue performance.

2.2. Reduction of defect size and change in defect shape

While HIP treatment does not remove defects, it can substantially reduce defect size [32, 36]. Textbook wisdom is that decreasing the size of fatigue crack initiating defects will improve fatigue performance [37], until a limit is reached where fatigue performance becomes controlled by other features. This has been observed in steels, aluminums, and brass, for defect sizes down to 10 – 100 μm depending upon the material and loading [37] (~ 10^7 life cycles). In titanium alloys, we are aware of no data that supports a relationship between individual defect size and high cycle fatigue performance for defect sizes below 200 μm [38].

In laser PBF Ti-6Al-4V, Leuders et al. [32] observed that the largest defects identified with X-ray CT were not responsible for fatigue failure, across as-built, heat-treated, and HIP treated cases. In the HIP treated case, defects of 100's of μm were found, yet fatigue failure initiated at α phase facets. In all cases, the failure initiated from defects or facets greater than 40 μm. In electron beam PBF Ti-6Al-4V, Tammas-Williams et al. [36] reported the same storyline, i.e. the largest defects were not ultimately responsible for fatigue failures and small defects, less than 5 μm, did not initiate fatigue cracks [20]. We note that these reports are consistent with the high cycle fatigue literature on conventionally cast Ti-6Al-4V, where Eylon [39] showed the most geometrically dominating defect (~ 1 mm) to not be associated with failure in HIP treated material.

As a whole, this data supports the idea that individual defects in Ti-6Al-4V can be of sufficient size to govern high cycle fatigue performance but still small enough to do so in a size independent manner. The bounds of this size range do vary among reports, but we contend that this is not surprisingly considering that variations in microstructure and loading can have a significant impact on high cycle fatigue behavior of Ti-6Al-4V [40]. The lack of

[1]While the interpretation of X-ray computed tomography data is not without its challenges and limitations [30, 31], at present we have no reason to suspect measurement/interpretation of artifacts would alter the conclusions reached in this manuscript.

defect size dependence across a greater range of sizes in Ti-6Al-4V is consistent with the importance of crack initiation in high cycle fatigue life in these alloys; relative to steels, aluminums, and brass, where short crack growth from defects determines high cycle fatigue life (~ 10^7 cycles) [37, 38]. The data of Masuo et al. [41] supports this assertion in that it shows a clear defect size dependence in PBF Ti-6Al-4V down to ~ 40 μm in low cycle fatigue tests ($\lesssim 10^5$ cycles) where crack growth is known to dominate life, even in Ti-6Al-4V.

Regarding the importance of defect shape, Zhang et al. [42] have shown that heat treatment can smooth the geometry of defects in laser PBF Ti-6Al-4V; yet, the fatigue performance of heat treated and as-built specimens is known to be indistinguishable when residual stresses do not govern [12, 13]. This point is consistent with traditional wisdom on aluminum and steels [37, 43], where only the projected area of the defect has a substantial effect on high cycle fatigue performance. Accordingly, we assume that defect shape is not a governing factor in high cycle fatigue performance within the context of this study. Nonetheless, we do note that such an assumption is expected to be invalid as defect size becomes large [44] and the concepts of traditional fracture mechanics become applicable.

Considering that the defects which lead to high cycle fatigue failure in well built PBF Ti-6Al-4V specimens tend to be below ~ 200 μm [12, 32, 36, 41], we assert that it would be inconsistent with available data to assume that defect size and shape play a substantial role in the high cycle fatigue performance of this material, with the constraint that defect size remains sufficient to initiate fatigue failure. In HIP treated laser PBF Ti-6Al-4V, we take this limit to be ~ 40 μm following [32].

2.3. Decrease in crack initiating defect population

While defect size and shape are not expected to be controlling parameters of Ti-6Al-4V high cycle fatigue performance, provided defect size is sufficient to initiate a fatigue crack (above ~ 40 μm), a general reduction in defect size will decrease the number of defects above ~ 40 μm; and thus, decrease the defect population that has been observed to initiate fatigue cracks, ultimately improve fatigue performance [12, 16]. We have examined this possibility with a simple model built upon three overarching assumptions.

First, in the context of the specimens and loadings considered here, the number of loading cycles to specimen failure (specimen fatigue life, N_f) can be accurately approximated as the number of cycles required to initiate a fatigue crack. Second, we assume that potential initiation sites act independently of each other. This implies that the survival probability of two sets of specimens, differing only by number of defects per specimen, are related by the ratio of defects between sets,

$$\mathrm{P}\left(\log_{10} N_f > \log_{10} n_f\right) = S_{\mathscr{A}}\left(\log_{10} n_f\right) = \left(S_{\mathscr{B}}\left(\log_{10} n_f\right)\right)^{\eta}, \quad (1)$$

with η representing the ratio of defects between sets. In other words, $\mathrm{P}(\log_{10} N_f > \log_{10} n_f)$ represents the probability that the logarithm of the randomly sampled fatigue life, N_f, is

greater than a specified logarithm of fatigue life, n_f. We have labeled the two sets of specimens that differ only by the number of defects per specimen as $\mathscr{A}$ and $\mathscr{B}$.

The first assumption is typical for high cycle fatigue studies. It was specifically tested for the fatigue data in Fig. 4, which is the basis for the conclusion of this section. Using finite element analysis [45], FRANC3D [46], and long crack growth data for 800 °C heat treated laser PBF Ti-6Al-4V (da/dN vs. ΔK_I) in [11], the number of cycles to grow a crack from 127 μm to 800 μm was predicted for a 3 mm round specimen. A loading amplitude of $\sigma_a = 404$ MPa was considered as a bounding case where the crack growth life has the most substantial contribution to the failure data in Fig. 4. The crack growth life was considered to be the number of cycles to grow a crack over the range that linear elastic fracture mechanics is valid following ASTM standard [47]. The number of loading cycles associated with crack growth above this range was considered minuscule, and the number of cycles associated with crack lengths below was considered to be associated with crack initiation processes. The range of stress intensity factors, $\Delta K_I = 5.1 - 16.2\ \mathrm{MPa}\sqrt{m}$, was within the range of the input crack growth data in [11], such that no extrapolation of crack growth data was required. The predicted value of linear elastic fatigue crack growth life was only 1 % of the fatigue life (~ 10 million cycles) for the heat treated failure data in Fig. 4. This percentage will decrease with loading amplitude and will be smaller for the HIP'd data in Fig. 4. Thus, the above calculation bounds the error of the first assumption and supports its use.

We contend that the second assumption is reasonable considering the length scales involved. The average spacing between defects, with sizes larger than 40 μm, is 280 μm in the Ti-6Al-4V specimens that we will ultimately study in this section. This is significantly greater than that required for appreciable elastic interactions between nucleating cracks; i.e. even when two coplanar penny cracks are separated by only one forth of their diameter, the amplification to the stress intensity factor is only ~ 6 % [48]. Further, the average defect spacing is considerably greater than the microstructural length scale (a domain size of ~ 60 μm [12]), meaning that defect interactions due to nonlocal micro-plasticity would likely be negligible. Or in other words, the mean free path for dislocations is expected to be substantially less than the distance between build defects.

With (1) the number of cycles to initiate a fatigue crack from a specific defect being an independent random variable, (2) the fatigue life of the specimen being the minimum crack initiation life of all its defects, and (3) the number of defects being substantially greater than unity, we view the data from the perspective of asymptotic order statistics [49]. From this vantage, the specimen survival function is taken to be

$$S_{\mathscr{A}}\left(\log_{10} n_f\right) = e^{-\left(\frac{\log_{10} n_f - \theta_{\mathscr{A}}}{\lambda_{\mathscr{A}}}\right)^{\kappa_{\mathscr{A}}}}. \quad (2)$$

For convenience, we have used the logarithm of the specimen fatigue life to be the random variable, $\log_{10} N_f$.

The shape parameter, $\kappa_{\mathscr{A}}$, is associated with the evolution of the failure rate with respect to $\log_{10} n_f$. The location parameter, $\theta_{\mathscr{A}}$, controls the minimum observable value of $\log_{10} N_f$, which in practice would arise from specimens with large visible defects being discarded before fatigue testing. The remaining parameter, $\lambda_{\mathscr{A}}$, controls the the variance of $\log_{10} N_f$.

The dependence of S on the relative number of fatigue crack initiating defects in a specimen can then be obtained by plugging Eq. 2 into Eq. 1,

$$S_{\mathscr{A}}\left(\log_{10} n_f\right) = \left(S_{\mathscr{B}}\left(\log_{10} n_f\right)\right)^{\eta} \qquad (3)$$

$$\left(\frac{\log_{10} n_f - \theta_{\mathscr{A}}}{\lambda_{\mathscr{A}}}\right)^{\kappa_{\mathscr{A}}} = \eta\left(\frac{\log_{10} n_f - \theta_{\mathscr{B}}}{\lambda_{\mathscr{B}}}\right)^{\kappa_{\mathscr{B}}}$$

$$\frac{\left(\log_{10} n_f - \theta_{\mathscr{A}}\right)^{\kappa_{\mathscr{A}}}}{\left(\log_{10} n_f - \theta_{\mathscr{B}}\right)^{\kappa_{\mathscr{B}}}} = \eta\frac{\lambda_{\mathscr{A}}^{\kappa_{\mathscr{A}}}}{\lambda_{\mathscr{B}}^{\kappa_{\mathscr{B}}}},$$

and noting that Eq. 3 applies for a range of n_f values, requiring $\kappa_{\mathscr{A}} = \kappa_{\mathscr{B}}$ and $\theta_{\mathscr{A}} = \theta_{\mathscr{B}}$. This reduces Eq. 3 to

$$\lambda_{\mathscr{A}} = \frac{\lambda_{\mathscr{B}}}{\eta^{\frac{1}{\kappa}}}. \qquad (4)$$

It is common for fatigue data to be collected across a range of loading magnitudes, e.g. σ_a. On a log-log axis, the data is often well described by a linear relationship, provided the dominating mechanism controlling fatigue life remains constant,

$$\mathbf{E}\left[\log_{10} N_f\right] = A_{\mathscr{A}}\log_{10}\sigma_a + B_{\mathscr{A}}, \qquad (5)$$

with **E** being the expectation operator. This relationship is traditionally referred to as an S-N or Wöhler curve. $A_{\mathscr{A}}$ and $B_{\mathscr{A}}$ are estimated by ordinary least squares linear regression of the collected failure data in a log-log space, e.g. $\log_{10} \sigma_a$ vs $\log_{10} N_f$. This approach assumes that the variance of $\log_{10} N_f$ is independent of $\log_{10} \sigma_a$, an assumption that is consistent with high cycle fatigue experimental data over ranges where the failure mechanism and S-N slope remain constant [50]. On this point, we note that some publications do show a stress dependent variance of fatigue life [51], but this occurs over a range where the slope of the S-N curve is not linear and multiple mechanisms are likely to act.

The stress independence of the variance of the fatigue life is the third assumption in the modeling framework. This assumption leads to $\kappa_{\mathscr{A}}$ and $\lambda_{\mathscr{A}}$ being stress independent, which becomes evident by considering that $\kappa_{\mathscr{A}}$ is independent of the number of defects in a specimen but not $\lambda_{\mathscr{A}}$:

$$\frac{\partial \mathrm{Var}\left(\log_{10} N_f\right)}{\partial \log_{10}\sigma_a} = 0 \qquad (6)$$

$$d\frac{\partial\left[\lambda_{\mathscr{A}}^2\left(\Gamma\left(2K_A - 1\right) - \left(\Gamma\left(K_A\right)\right)^2\right)\right]}{\partial \log_{10}\sigma_a} = 0$$

$$\frac{1}{\lambda_{\mathscr{A}}}\frac{\partial \lambda_{\mathscr{A}}}{\partial \log_{10}\sigma_a} - \frac{1}{\kappa_{\mathscr{A}}^2}\frac{\partial \kappa_{\mathscr{A}}}{\partial \log_{10}\sigma_a}\frac{\frac{\partial\Gamma\left(2K_A - 1\right)}{\partial\left(2K_A - 1\right)} - \Gamma\left(K_A\right)\frac{\partial\Gamma\left(K_A\right)}{\partial\left(K_A\right)}}{\Gamma\left(2K_A - 1\right) - \left(\Gamma\left(K_A\right)\right)^2} = 0,$$

where $K_A = 1 + \frac{1}{\kappa_{\mathscr{A}}}$.

The stress independence of $\kappa_{\mathscr{A}}$ and $\lambda_{\mathscr{A}}$ implies that the stress dependence of the fatigue life distribution must arise entirely through $\theta_{\mathscr{A}}$. We contend that this conclusion is consistent with the mechanistic origins of $\kappa_{\mathscr{A}}$, $\lambda_{\mathscr{A}}$, and $\theta_{\mathscr{A}}$ when the distribution of fatigue life is far above zero, i.e. high cycle regime. The conclusion implies identically sloped S-N curves for sets of specimens (e.g. $\mathscr{A}$ and $\mathscr{B}$) that only differ by their number of defects; considering

$$\frac{\partial \mathbf{E}\left(\log_{10} N_f\right)}{\partial \log_{10}\sigma_a} = \frac{\partial\left(\theta_{\mathscr{A}} + \lambda_{\mathscr{A}}\Gamma\left(1 + \frac{1}{\kappa_{\mathscr{A}}}\right)\right)}{\partial \log_{10}\sigma_a} = \frac{\partial\left(A_{\mathscr{A}}\log_{10}\sigma_a + B_{\mathscr{A}}\right)}{\partial \log_{10}\sigma_a} \qquad (7)$$

together with the stress independence of $\kappa_{\mathscr{A}}$, $\lambda_{\mathscr{A}}$, and $B_{\mathscr{A}}$, which gives

$$\frac{\partial \theta_{\mathscr{A}}}{\partial \log_{10}\sigma_a} = A_{\mathscr{A}}, \qquad (8)$$

which shows that $A_{\mathscr{A}}$ is independent of the number of defects in the specimen, i.e. $A_{\mathscr{A}} = A_{\mathscr{B}}$, via $\theta_{\mathscr{A}} = \theta_{\mathscr{B}}$.

Schweiger and Heckel [52] have generated high cycle fatigue data that is controlled by crack initiation and can be used to validate the modeling framework introduced to this point. Their work is rare in that it was a study specifically aimed at fatigue life distribution. Schweiger

and Heckel's data corresponds to the results of a large number of high cycle fatigue tests on sets of aluminum specimens that only differed by the number of macroscopically drilled holes in a specimen. Here we consider two sets of specimens having either 1 or 7 drilled holes of equal characteristics. Considering that fatigue cracks initiate from defects in the vicinity of the holes, the sets of specimens can be interpreted as differing by the number of potential crack initiating defects. We first computed the mean logarithm fatigue life $\log_{10} N_f$ for the two sets of specimen data, and then chose the only free parameter κ governing $S_{\mathscr{A}}\left(\log_{10} n_f\right)$ and $S_{\mathscr{B}}\left(\log_{10} n_f\right)$ by a simultaneous least squares fit to the corresponding estimators, $\hat{S}_{\mathscr{A}}\left(\log_{10} N_f\right)$ and $\hat{S}_{\mathscr{B}}\left(\log_{10} N_f\right)$, in a linearized space, e.g. $\ln(\log_{10} N_f - \theta)$ vs $\ln(\ln(S^{-1}))$, where κ is the slope and λ is the exponent of the negative intercept over κ. Corresponding to the two sets of specimens, η is taken to be 7. The small sample sizes of subsequently presented data sets and the intuitive graphical nature of the least squares regression approach motivated its use over maximum likelihood parameter estimation. $\hat{S}_{\mathscr{A}}\left(\log_{10} N_f\right)$ and $\hat{S}_{\mathscr{B}}\left(\log_{10} N_f\right)$ were taken to be Kaplan-Meier estimators [53].

As shown in Fig. 2, the distribution of fatigue life for the seven and single holed specimens can be well fit by the model introduced in this section, with R^2 values of 0.98 and 0.92 respectively. The fit model parameters are $\theta = 4.93$, $\lambda_{\mathscr{A}} = 1.08$, $\lambda_{\mathscr{B}} = 1.42$ and $\kappa = 7.29$. The ability of the model to fit the data shown in Fig. 2 supports its application in contexts where the difference in fatigue performance between two sets of specimens is governed by differences in fatigue crack initiating defect populations.

The application of the theoretical framework to stress dependent data is validated using the data set of Shirani and Härkegård [54]. These authors examined the fatigue life of two sets of ductile cast iron specimens, differing in size. Noting that all failures were surface initiated, the ratio in the surface area of the gage sections was considered equivalent to the ratio of fatigue crack initiating defects between the two sets of specimens. Accordingly, $\eta = 5.98$ in this case. Other size effects resulting from differences in strain gradients and material microstructure were assumed negligible. As shown in Fig. 3a, log-log least squares regression was performed on the S-N curves for both data sets to estimate $A_{\mathscr{A}}$, $B_{\mathscr{A}}$, $A_{\mathscr{B}}$, and $B_{\mathscr{B}}$ with the constraint that $A_{\mathscr{A}} = A_{\mathscr{B}} = A$, referring to the large specimens as set $\mathscr{A}$ and the small specimens as set $\mathscr{B}$. With the values of A, $B_{\mathscr{A}}$, and $B_{\mathscr{B}}$ determined, only a single free parameter κ remains in the model. This parameter is chosen by a simultaneous least squares fit of $S_{\mathscr{A}}\left(\log_{10} n_f\right)$ and $S_{\mathscr{B}}\left(\log_{10} n_f\right)$ to the corresponding estimators, $\hat{S}_{\mathscr{A}}\left(\log_{10} N_f\right)$ and $\hat{S}_{\mathscr{B}}\left(\log_{10} N_f\right)$, in a linearized space. The fit resulted in $\theta = 0.0$, $\lambda_{\mathscr{A}} = 4.7$, $\lambda_{\mathscr{B}} = 5.0$ and $\kappa = 27.6$, which yielded R^2 values of 0.82 and 0.76 respectively (Fig. 3b). Considering (1) the small number of samples in each data set, (2) the potential importance that crack growth might play in this study relative to crack initiation, and (3) the effects of different cooling rates in the small and large specimens during casting (which would create different microstructures); the model captures the relation between the fatigue life and the number of fatigue crack initiating defects relatively well.

For the laser PBF case, the data of Günther et al. [19] was examined, as it provides S-N data for laser PBF Ti-6Al-4V after both a 800 °C heat treatment and a 920 °C HIP treatment. While the difference in defect population between these two sets of specimens was not measured, the same research group [32] has quantified the difference in the defect population between as-built and HIP treated conditions for specimens printed on the same machine with the same build parameters. Considering the experimental data in [11, 13, 55], we assume that a 800 °C heat treatment does not influence the defect population relative to the as-built condition. Thus, we took the ratio of the number of defects above 40 μm in heat treated and HIP treated specimens to be 8.6 from the data presented in Leuders et al. [32].

As done in the validation cases, log-log least squares regression was utilized to find $A_{\mathscr{A}}$, $B_{\mathscr{A}}$, $A_{\mathscr{B}}$, and $B_{\mathscr{B}}$ for Günther et al.'s fatigue data [19], with the constraint that $A_{\mathscr{A}} = A_{\mathscr{B}} = A$ and referring to the heat treated specimens as set $\mathscr{A}$ and the HIP treated specimens as set $\mathscr{B}$ (Fig. 4a). Censored data was included in the fit via the in-out method [56]. The censored data included run-outs at low stress levels and surface initiated failures at high stress levels. With $A_{\mathscr{A}}$, $B_{\mathscr{A}}$, $A_{\mathscr{B}}$, and $B_{\mathscr{B}}$ obtained, the fatigue data of each set was collapsed to the maximum stress level of the uncensored data, σ_a = 561 MPa.

Then, as done previously, we chose the remaining free parameter κ governing $S_{\mathscr{A}}\left(\log_{10} n_f\right)$ and $S_{\mathscr{B}}\left(\log_{10} n_f\right)$ by a simultaneous least squares fit to the corresponding estimators in a linearized space. Fitting both the heat treated and the HIP treated specimen data gave θ = 1.46, $\lambda_{\mathscr{A}}$ = 4.22, $\lambda_{\mathscr{B}}$ = 6.61 and κ = 4.79, which yielded R^2 values of 0.87 and 0.37 respectively (Fig. 4b). The inability of the model to accurately fit the data suggests that the difference in fatigue performance between the two sets of specimens cannot be solely attributed to a difference in fatigue initiating defect population[2]. In other terms, the model and the data in Fig. 4 show that the variability in the collected fatigue life data would need to be much larger for differences in defect population to explain the difference in fatigue performance between the HIP'd and heat treated specimens.

The data in Fig. 1 is consistent with this assertion. It does not suggest the fatigue performance of HIP'd specimens to depend on the quality of the specimens prior to HIP treatment. In other words, Fig. 1 suggests that a fractional reduction of the original fatigue crack initiating defect population by HIP does not explain the gains in fatigue performance due to HIP treatment.

2.4. Improvement of material microstructure

It is well established that HIP treatment of laser PBF Ti-6Al-4V evolves the microstructure. Under the typical process route, the fine (~ 500 nm) lamellar martensitic (α') structure changes to a coarsened α lamellar structure with ~ 3 μm lamellae thicknesses and ~ 60 μm lengths (noting that the latter number depends on the cooling rate from the HIP soak temperature) [6, 12, 13, 16]. Published SEM micrographs of HIP'd laser PBF Ti-6Al-4V

[2]We note that this conclusion is only made stronger if the 3 most outlying points in the heat treated data in Fig. 4b are removed from the fitting procedure.

appear similar to those of heat treated laser PBF Ti-6Al-4V [12], suggesting that the pressure associated with HIP treatment does not play a role in the microstructural evolution[3]. Yet, there is a substantial difference in fatigue performance between HIP'd and heat treated specimens that have experienced similar thermal histories [12], which we have shown in the previous section cannot be explained by differences in the defect populations/characteristics. Following these points, we contend that a significant factor contributing to the improvement in fatigue performance of HIP'd specimens may be that the evolution of the microstructure near defects is different in HIP'd cases than heat treated cases. This observation is not to be expected from existing micrographs of HIP'd and heat treated microstructures, because the microstructure near defects was not specifically sought out (considering the average spacing between defects and the field of view of published micrographs). Noting the substantial change in defect volume that occurs during HIP treatment, appreciable plastic deformation near defects would be a likely driver of a difference in microstructure near defects.

3. Characterization of microstructure surrounding defects in HIP'd Ti-6Al-4V

Motivated by the outcome of the previous section, the microstructure near defects in laser PBF Ti-6Al-4V was examined via EBSD microscopy. Cylindrical specimens with a length of 160 mm and a diameter of 12 mm were built in a vertical orientation at Incodema3D on an EOS M280 machine with default settings (e.g. 260 W laser power, 1.2 m/s scan speed, 30 μm layer thickness, and 140 μm hatch spacing) from TEKMAT Ti64–53/20 powder. After the build, specimens were heated treated in vacuum by Bodycote: 650 ± 25 °C for 180 ± 15 min, followed by air cool. Finally the specimens were HIP treated at Quintus Technologies: 920 °C and 100 MPa for 120 min, then cooled at 5 °C/min and depressurized at 0.3 MPa/min for 140 min.

Prior to HIP treatment, X-ray computed tomography was performed on a Zeiss Versa 520 micro-CT system with an acceleration voltage of 140 kV, current of 71.6 μA, and power of 10 W. 1601 projections were collected on a scintillator detector while the sample was rotated 360° at 4 – 5 s exposure time. Low density regions of eight or more contiguous voxels were classified as defects. With this definition and a 7 μm voxel size, 713 defects were detected in a 317 mm^3 volume prior to HIP treatment. After HIP treatment, no defects were detected following the same procedure. For reference, a sphere of 17 μm diameter would occupy the volume of eight 7 μm voxels.

Specimens were sectioned perpendicular to the build axis and mechanically polished for EBSD orientation mapping. The EBSD analysis of the sectioned surface away from its edges showed the expected basketweave microstructure (Fig. 5a&b). Considering the 862 grains captured in two images/locations, the average lengths of the long and short axis of the α grains on the sectioned surface were 10.5 and 2.2 μm. The length of the long axis of the α grains is shown in Fig. 5c. Consistent with existing literature, build defects were absent in

[3]Noting that a careful comparison of HIP'd and heat treated laser PBF Ti-6Al-4V microstructures is not yet available.

the images of random locations on the cross section, due to the low number density of defects, i.e. 713 defects per 317 mm^3, equivalent to 1 defect per ~ 1 cm^2 of cross section assuming defect diameters of ~ 5 μm after HIP. An extensive search in the HIP'd material located 3 defects with sizes of 5.1, 6.5 and 2.8 μm (Fig. 6a,b&c). The microstructure surrounding thees three defects was characterized by the long axis length of α grains and their proximity to the center of the defect. The lengths of the long axis of the grains are shown in Fig. 6d. Comparing to the data obtained in Fig. 5a&b, there appears to be a lack of large grains in the vicinity of the defects.

To better establish this point, the observation of α grain size was considered as a Bernoulli variable, whereby grains having a long axis greater than 12 μm were classified as long. No long grains were found to reside within 18 μm of the three defects examined (0 out of 244); yet, away from defects, 28 % of the grains were long (241 out of 862). 18 μm represents about twice the global averaged length of the long axis of grains. As a null hypothesis we considered the two sets of data to be independent samples from the same probability distribution. In this case, the estimated probability of observing a long grain in a micrograph of HIP'd material is 22 %. This implies that the probability of randomly observing no long grains (or an equal or greater fluctuation from the expectation) within 18 μm of defects is 2.6E-14 in a sample size of 244. Thus, the null hypothesis is very unlikely given the EBSD observations made here. In other words, it is very likely that the distribution of grain size near defects is substantially different than the distribution of grain size away from defects in the HIP'd material.

Examination of the microstructure prior to HIP treatment supports that it is the HIP process that makes the microstructure near defects substantially different from the bulk. Examining the microstructure near 3 defects prior to HIP treatment (Fig. 7), 22 of 143 grains were classified as long, within 18 μm of defects. At distances beyond 18 μm from defects, 104 of 475 grains were classified as long. Not too different than the HIP'd case, the estimated probability of observing a long grain in a micrograph prior to HIP treatment is 20 %, assuming both samples are from the same distribution. Consequently, the probability of randomly observing ≤ 22 long grains within 18 μm of defects (or an equal or greater fluctuation from the expectation) is 21 % in a sample size of 143. Thus, the data does not support the rejection of the argument that the microstructure near defects is similar to that away from defects prior to HIP treatment. This supports the assertion that the difference in microstructure near defects in the HIP'd material is due to the HIP process.

The above finding is consistent with literature on HIP compaction of Ti-6Al-4V powder. Guo et al., Zhang et al., and Cai et al. [57–60] have each independently observed a fine equiaxed microstructure in the consolidated material at locations where powder particles had fused together. This contrasted the widespread lamellar microstructure (similar to that of the starting powder) that was observed at other locations that presumably underwent substantially less deformation during compaction. This transition from lamellar to more equiaxed microstructure is also apparent near the HIP'd defects identified in this work (Fig. 6a). Furthermore, in traditional Ti-6Al-4V, Eylon [39] has shown a substantial difference in microstructure between two locations in a HIP'd casting. One location was near a previously mm sized pore and the other was in a region having no observable porosity prior to HIP

treatment. The chemistry at both locations was found to be not significantly different, suggesting the differences in post HIP'd microstructure were due to the plastic deformation that occurred near the pore during HIP treatment.

The deformation that occurs near defects or at the interfaces of prior powder particles during HIP has similarities to the typical processing route used for wrought Ti-6Al-4V. In both cases, substantial deformation in the $\alpha+\beta$ temperature range occurs. Traditionally, hot working of Ti-6Al-4V is known to improve high cycle fatigue performance by creating a microstructure that is less susceptible to fatigue crack initiation [8, 61, 62]. On this point, Semiatin et al. [63] have examined the strain and temperature required to globularize Ti-6Al-4V lamellar microstructures. The required conditions are well within what might be expected to occur near defects during standard HIP processing. Further, Perumal et al. [64] have shown that such microstructural transformations are also possible when starting from a martensitic microstructure, which is more similar to the HIP treatment of PBF Ti-6Al-4V.

In summary, our EBSD observations show the microstructure evolves differently near defects during HIP treatment. We have used the long axis of α grains to characterize the microstructure, but note that other attributes may be distinguishable as well, e.g. aspect ratio, texture, volume fraction of β phase[4]. This finding is consistent with previous reports on powder compaction and traditionally cast Ti-6Al-4V, and is congruent with the traditional wisdom that deformation can induce microstructural evolution. While there are several reasons to believe that the hot worked microstructure near defects will inhibit fatigue crack initiation (as with wrought Ti-6Al-4V [40, 61, 62, 64]), more work is required to firmly establish this final point.

4. Modeling the role of HIP on high cycle fatigue performance

A comprehensive understanding of the relationship between defects, microstructure, and high cycle performance remains an ongoing research challenge. Accordingly, it is not yet feasible to comprehensively predict high cycle fatigue performance from HIP treatment parameters. Nonetheless, some guidance on parameter selection can be given. From a high cycle fatigue perspective, the goal of HIP treatment is to neutralize subsurface crack initiating defects. The optimum HIP parameters will achieve this goal while minimizing detrimental microstructural coarsening [8–13]. Accordingly, the optimum HIP treatment parameters correspond to the minimum soak temperature and time required for HIP treatment to neutralize crack initiating defects at the maximum pressure capacity of the HIP chamber.

Building from the previous sections, we assert that the neutralization of fatigue crack initiating defects requires a reduction in defect size, either to sizes below ~ 40 μm or to the extent that the microstructure surrounding the defect evolves sufficiently to neutralize fatigue crack initiation. The latter case is considered here in that it is independent of as-built defect sizes, and thus provides a conservative bound on optimum/minimum HIP parameters

[4]Noting that in all EBSD observations the volume fraction of β phase was found to be less than 6 % and disregarded in the orientation maps for simplicity.

(for cases where initial sizes of failure causing defects are below an upper bound, $\lesssim 200$ μm). As a conservative guess, we consider an 80 % decrease in defect diameter to be effective in neutralizing defects with respect to fatigue crack initiation. For laser PBF Ti-6Al-4V, the data available in existing literature shows that a 33 % to 50 % decrease in defect diameter is sufficient for neutralizing crack initiating defects [12, 32]. Regardless, the recommendations are relatively insensitive to this value given the shape of the curves in Fig. 8.

We describe the action of HIP treatment on defect size using a simple continuum mechanics model introduced by Wilkinson and Ashby [65]. Considering an infinite nonlinear viscous medium under hydrostatic stress, the volume of a spherical defect/void follows [66]

$$\dot{V} = -\frac{3}{2}SA\left(\frac{3|\Delta P|}{2n}\right)^n V, \quad (9)$$

where $\Delta P = P_e - P_i$ is the difference between external P_e and internal pressure P_i of the defect, | | is the absolute value operator, S is the sign of ΔP, V is the current volume of the spherical defect, A and n are the material parameters associated with the constitutive law, i.e. $\dot{\epsilon} = A\sigma^n$ for a uniaxial strain rate, $\dot{\epsilon}$, and stress state, σ. For the defect sizes relevant to fatigue crack initiation, the role of surface energy can be neglected without loss in accuracy [33, 65].

The spherical defect case is particularly useful in that it bounds the evolution of all defect morphologies. Specifically, Lee and Mear [66] have shown that for a nonlinear viscous material under hydrostatic stress, the volumetric strain rate for both oblate and prolate defects exceeds that for a spherical defect. Thus, the evolution of the spherical defect is a conservative bound on the effectiveness of HIP treatment to improve fatigue performance.

While Eq. 9 applies directly to argon filled pore defects, lack of fusion defects containing unmelted powder particles are also common in as-built PBF materials. The consolidation of these defects parallels powder sintering, a process which has also been well described by continuum mechanics following Wilkinson and Ashby [65]. Using the simplifications of Helle et al. [67], the lack of fusion defects with interior filled by powders are predicted to evolve from their starting relative density of ~ 0.63 to ~ 0.9 in a small fraction of the time required for the remainder of the densification. When the interior of lack of fusion defects reaches a density of ~ 0.9, they will consist of distinct gas pore defects with dimensions less than the powder diameter, likely making them inert to fatigue crack initiation. Considering this point together with the prediction that the initial stages of consolidation inside lack of fusion defects proceed quickly, the parameters governing an effective HIP treatment are dictated by the closure of gas pore type defects.

To apply Wilkinson and Ashby's model [65, 66] to simulate defect evolution during HIP of laser PBF Ti-6Al-4V, the material constants, A and n, are needed. There is considerable uncertainty in the choice of these parameters, as they depend on the microstructure, temperature, strain rate, and strain during tests. Considering the available literature and the

timescales associated with the HIP process, we focus on strain rates between 0.0003 s^{-1} and 0.01 s^{-1}. Fitting to available data in [64, 68–71], Table 1 has been constructed to convey the range of values that the governing material parameters might take when considering HIP treatment of laser PBF Ti-6Al-4V.

For each case in Table 1, the evolution of a spherical argon filled defect is predicted following Eq. 9, again noting that this conservatively bounds the effectiveness that one might expect from HIP treatment on a population of defects having various characteristics, including those in electron beam PBF. HIP pressures of 100 and 200 MPa were considered and the initial pressure inside the defect was taken to be the atmospheric value of 0.1 MPa, following our understanding of typical laser PBF machines and gas atomization chambers for Ti-6Al-4V powders [20]. To convey the nature of defect size evolution and its dependence on the relevant parameters, results for several cases are displayed in Fig. 8. Noting that internal pressure will equilibrate with external pressure at a 90 % decrease in diameter with a HIP pressure of 100 MPa and 92 % with 200 MPa, the curves illustrate that the majority of defect closure of ~ 80 % occurs quick relative to its final stages.

Using the parameter constants in Table 1, the times required to obtain the initial rapid decrease in defect diameter of 80 % are plotted on a time/temperature map (Fig. 9). The data points corresponding to 100 and 200 MPa HIP soak pressures are encapsulated by a shaded region to give an overall sense of the predictions. If one considers a decrease in defect diameter of > 80 % to be sufficient for neutralizing defects with respect to high cycle fatigue crack initiation, the map can then be interpreted as providing guidance for minimum HIP treatment temperatures given the pressure capacity of the furnace and the budgeted time (with times and temperatures to the upper right of the shaded regions being sufficient for effective HIP treatment of defects). The traditionally recommended ASTM HIP parameters (represented by the gray shaded region in Fig. 9) are consistent with the predictions [3].

5. Summary and conclusions

In total, published laboratory test results of multiple independent research groups have established a post processing route (HIP + subsequent surface treatment) capable of producing laser PBF Ti-6Al-4V with high cycle fatigue performance on par with traditional wrought processed material. Contrary to statements published elsewhere, the open literature (and the microscopy performed here) suggests that subsurface defects are not eliminated by successful HIP treatments. With that said, it is indisputable that the size of defects is decreased by HIP treatment. While in some cases successful HIP treatment reduces the size of all defects below a critical limit where they can no longer dictate high cycle fatigue life, this is not universally true. In other words, HIP treatment can yield good high cycle fatigue performance without decreasing the size of all defects below a critical limit. Moreover, we find that changes in the number of defects of size sufficient to nucleate fatigue cracks cannot explain the performance gain associated with HIP treatment (utilizing a weakest link model to analyze published fatigue performance data relative to defect size distributions). These results motivated a hypothesis that the microstructure evolves differently near defects during HIP treatment, considering that heat treatment alone has been shown to not improve high cycle fatigue performance when controlled by defects. This hypothesis is confirmed by the

examination of EBSD microscopy. Using the maximum length of α grains as the distinguishing characteristic, we found the microstructure to be more refined near defects. This finding has several implications. First, qualification of fatigue critical parts will be conservative if based solely on defect size, i.e. a HIP'd part might display large defects (~ 40 μm to ~ 200 μm) but have good high cycle fatigue performance. Second, the selection of build parameters that do not necessarily minimize defect populations might provide a benefit when HIP post processing is used. Specifically, an increased population of build defects might lead to a greater fraction of material with a refined microstructure after HIP. Third, the optimum HIP parameters (those which coarsen the microstructure away from defects the least, while still neutralizing crack initiating defects) are determined by considering the local strain required to neutralize defects during HIP treatment. A model built upon the third point was found to predict HIP parameters consistent with the standard practice, and suggests parameter combinations that might be useful when moving to longer HIP soak times and HIP chambers with greater pressure capacities.

Acknowledgements

DHW acknowledges financial support from ONR contract #N000141712035, the Cornell University Biotechnology Resource Center for X-ray microscopy support via NIH 1S10OD012287, Technical Data Analysis for supplying the EBSD specimens, Mircea Grigoriu for technical advice on the probabilistic aspects of the paper, and Quintus Technologies for providing the HIP treatment of the specimens.

References

[1]. Li P, Warner DH, Fatemi A, and Phan N. Critical assessment of the fatigue performance of additively manufactured Ti-6Al-4V and perspective for future research. International Journal of Fatigue, 85:130–143, 2016.

[2]. Atkinson HV and Davies S. Fundamental aspects of hot isostatic pressing: an overview. Metallurgical and Materials Transactions A, 31(12):2981–3000, 2000.

[3]. ASTM F2924–14 Standard Specification for Additive Manufacturing Titanium-6 Aluminum-4 Vanadium with Powder Bed Fusion. ASTM International, West Conshohocken, PA, 2014 10.1520/F2924.

[4]. Titanium Alloy Castings, Investment 6Al - 4V Hot Isostatic Pressed, Anneal Optional. AMS, 1980 10.4271/AMS4991.

[5]. Metallic Materials Properties Development and Standardization (MMPDS-05). Battelle Memorial Institute, 2010.

[6]. Wycisk E, Siddique S, Herzog D, Walther F, and Emmelmann C. Fatigue performance of laser additive manufactured Ti-6Al-4V in very high cycle fatigue regime up to 109 cycles. Frontiers in Materials, 2:72, 2015.

[7]. Seifi M, Salem A, Satko D, Shaffer J, and Lewandowski JJ. Defect distribution and microstructure heterogeneity effects on fracture resistance and fatigue behavior of EBM Ti-6Al-4V. International Journal of Fatigue, 94:263–287, 2017.

[8]. Lütjering G and Williams JC. Titanium. Springer, 2007.

[9]. Rekedal KD and Liu D. Fatigue life of selective laser melted and hot isostatically pressed Ti-6Al-4V absent of surface machining. In Proceedings of the 56th AIAA/ASCE/AHS/ASC structures, structural dynamics, and materials conference, Kissimmee, FL, 2015.

[10]. Rafi HK, Starr TL, and Stucker BE. A comparison of the tensile, fatigue, and fracture behavior of Ti-6Al-4V and 15–5 PH stainless steel parts made by selective laser melting. The International Journal of Advanced Manufacturing Technology, 69(5–8):1299–1309, 2013.

[11]. Leuders S, Tho¨ne M, Riemer A, Niendorf T, Tröster T, Richard HA, and Maier HJ. On the mechanical behaviour of titanium alloy TiAl6V4 manufactured by selective laser melting:

Fatigue resistance and crack growth performance. International Journal of Fatigue, 48:300–307, 2013.

[12]. Kasperovich G and Hausmann J. Improvement of fatigue resistance and ductility of TiAl6V4 processed by selective laser melting. Journal of Materials Processing Technology, 220:202–214, 2015.

[13]. Leuders S, Lieneke T, Lammers S, Tröster T, and Niendorf T. On the fatigue properties of metals manufactured by selective laser melting-the role of ductility. Journal of Materials Research, 29(17):1911–1919, 2014.

[14]. Siddique S, Imran M, Rauer M, Kaloudis M, Wycisk E, Emmelmann C, and Walther F. Computed tomography for characterization of fatigue performance of selective laser melted parts. Materials and Design, 83:661–669, 2015.

[15]. Quintus Technology. The ultimate heat treatment solution brochure, 2018.

[16]. Zhao X, Li S, Zhang M, Liu Y, Sercombe TB, Wang S, Hao Y, Yang R, and Murr LE. Comparison of the microstructures and mechanical properties of Ti-6Al-4V fabricated by selective laser melting and electron beam melting. Materials and Design, 95:21–31, 2016.

[17]. Greitemeier D, Palm F, Syassen F, and Melz T. Fatigue performance of additive manufactured TiAl6V4 using electron and laser beam melting. International Journal of Fatigue, 94:211–217, 2017.

[18]. Walker K. The effect of stress ratio during crack propagation and fatigue for 2024-T3 and 7075-T6 aluminum. In Effects of environment and complex load history on fatigue life. ASTM International, 1970.

[19]. Günther J, Krewerth D, Lippmann T, Leuders S, Tro¨ster T, Weidner A, Biermann H, and Niendorf T. Fatigue life of additively manufactured Ti-6Al-4V in the very high cycle fatigue regime. International Journal of Fatigue, 94:236–245, 2017.

[20]. Tammas-Williams S, Withers PJ, Todd I, and Prangnell PB. The effectiveness of hot isostatic pressing for closing porosity in titanium parts manufactured by selective electron beam melting. Metallurgical and Materials Transactions A, 47(5):1939–1946, 2016.

[21]. Edwards P and Ramulu M. Fatigue performance evaluation of selective laser melted Ti–6Al–4V. Materials Science and Engineering: A, 598:327–337, 2014.

[22]. Gong H, Rafi K, Gu H, Ram GDJ, Starr T, and Stucker B. Influence of defects on mechanical properties of Ti–6Al–4V components produced by selective laser melting and electron beam melting. Materials & Design, 86:545–554, 2015.

[23]. Wycisk E, Solbach A, Siddique S, Herzog D, Walther F, and Emmelmann C. Effects of defects in laser additive manufactured Ti-6Al-4V on fatigue properties. Physics Procedia, 56:371–378, 2014.

[24]. Liu QC, Elambasseril J, Sun SJ, Leary M, Brandt M, and Sharp PK. The effect of manufacturing defects on the fatigue behaviour of Ti-6Al-4V specimens fabricated using selective laser melting. In Advanced Materials Research, volume 891, pages 1519–1524. Trans Tech Publ, 2014.

[25]. Velisavljevic N, MacLeod S, and Cynn H. Titanium alloys at extreme pressure conditions. In Titanium Alloys-Towards Achieving Enhanced Properties for Diversified Applications. InTech, 2012.

[26]. Wu MW and Lai PH. The positive effect of hot isostatic pressing on improving the anisotropies of bending and impact properties in selective laser melted Ti-6Al-4V alloy. Materials Science and Engineering: A, 658:429–438, 2016.

[27]. Qiu C, Adkins NJE, and M Attallah M. Microstructure and tensile properties of selectively laser-melted and of HIPed laser-melted Ti-6Al-4V. Materials Science and Engineering: A, 578:230–239, 2013.

[28]. Shui X, Yamanaka K, Mori M, Nagata Y, Kurita K, and Chiba A. Effects of post-processing on cyclic fatigue response of a titanium alloy additively manufactured by electron beam melting. Materials Science and Engineering: A, 680:239–248, 2017.

[29]. Lu SL, Tang HP, Ning YP, Liu N, StJohn DH, and Qian M. Microstructure and mechanical properties of long Ti-6Al-4V rods additively manufactured by selective electron beam melting out of a deep powder bed and the effect of subsequent hot isostatic pressing. Metallurgical and Materials Transactions A, 46(9):3824–3834, 2015.

[30]. Hermanek P and Carmignato S. Porosity measurements by x-ray computed tomography: Accuracy evaluation using a calibrated object. Precision Engineering, 49:377–387, 2017.

[31]. Thompson A, Maskery I, and Leach RK. X-ray computed tomography for additive manufacturing: a review. Measurement Science and Technology, 27(7):072001, 2016.

[32]. Leuders S, Vollmer M, Brenne F, Tröster T, and Niendorf T. Fatigue strength prediction for titanium alloy TiAl6V4 manufactured by selective laser melting. Metallurgical and Materials Transactions A, 46(9):3816–3823, 2015.

[33]. Shao S, Mahtabi MJ, Shamsaei N, and Thompson SM. Solubility of argon in laser additive manufactured α-titanium under hot isostatic pressing condition. Computational Materials Science, 131:209–219, 2017.

[34]. Cunningham R, Nicolas A, Madsen J, Fodran E, Anagnostou E, Sangid MD, and Rollett AD. Analyzing the effects of powder and post-processing on porosity and properties of electron beam melted Ti-6Al-4V. Materials Research Letters, 5(7):516–525, 2017.

[35]. Tammas-Williams S, Withers PJ, Todd I, and Prangnell PB. Porosity regrowth during heat treatment of hot isostatically pressed additively manufactured titanium components. Scripta Materialia, 122:72–76, 2016.

[36]. Tammas-Williams S, Withers PJ, Todd I, and Prangnell PB. The influence of porosity on fatigue crack initiation in additively manufactured titanium components. Scientific Reports, 7, 2017.

[37]. Murakami Y. Metal fatigue: effects of small defects and nonmetallic inclusions. Elsevier, 2002.

[38]. Matsunaga H, Murakami Y, Kubota M, and LEE JH. Fatigue strength of Ti-6Al-4V alloys containing small artificial defects. Journal of the Society of Materials Science, Japan, 52(12Appendix):263–269, 2003.

[39]. Eylon D. Fatigue crack initiation in hot isostatically pressed Ti-6Al-4V castings. Journal of Materials Science, 14(8):1914–1922, 1979.

[40]. Pilchak AL, Williams REA, and Williams JC. Crystallography of fatigue crack initiation and growth in fully lamellar Ti-6Al-4V. Metallurgical and Materials Transactions A, 41(1):106, 2010.

[41]. Masuo H, Tanaka Y, Morokoshi S, Yagura H, Uchida T, Yamamoto Y, and Murakami Y. Effects of defects, surface roughness and hip on fatigue strength of Ti-6Al-4V manufactured by additive manufacturing. Procedia Structural Integrity, 7:19–26, 2017.

[42]. Zhang B, Ham K, Shao S, Shamsaei N, and Thompson SM. Effect of heat treatment and hot isostatic pressing on the morphology and size of pores in additive manufactured Ti-6Al-4V parts.

[43]. Gao YX, Yi JZ, Lee PD, and Lindley TC. The effect of porosity on the fatigue life of cast aluminium-silicon alloys. Fatigue and Fracture of Engineering Materials and Structures, 27(7): 559–570, 2004.

[44]. Kabir MR and Richter H. Modeling of processing-induced pore morphology in an additively-manufactured Ti-6Al-4V alloy. Materials, 10(2):145, 2017.

[45]. ABAQUS. 6.14 documentation. Dassault Systemes Simulia Corporation, 2014.

[46]. Ingrafea T et al. Franc3d, 3d fracture analysis code The Cornell University Fracture Group, Cornell University, Ithaca, NY, 1996.

[47]. ASTM E399–17 standard test method for linear-elastic plane-strain fracture toughness KIc of metallic materials, ASTM International, West Conshohocken, PA 2017.

[48]. Kachanov M and Laures JP. Three-dimensional problems of strongly interacting arbitrarily located penny-shaped cracks. International Journal of Fracture, 41(4):289–313, 1989.

[49]. Galambos J. The asymptotic theory of extreme order statistics. In The Theory and Applications of Reliability with Emphasis on Bayesian and Nonparametric Methods, pages 151–164. Elsevier, 1977.

[50]. Shimokawa T and Hamaguchi Y. Relationship between fatigue life distribution, notch configuration, and SN curve of a 2024-T4 aluminum alloy. Journal of Engineering Materials and Technology, 107(3):214–220, 1985.

[51]. Sinclair GM and Dolan TJ. Effect of stress amplitude on statistical variability in fatigue life of 75S-T6 aluminum alloy. Trans. ASME, 75:867, 1953.

[52]. Schweiger G and Heckel K. Size effect in randomly loaded specimens. International journal of fatigue, 8(4):231–234, 1986.

[53]. Kaplan EL and Meier P. Nonparametric estimation from incomplete observations. Journal of the American statistical association, 53(282):457–481, 1958.

[54]. Shirani M and Härkegård G. Fatigue life distribution and size effect in ductile cast iron for wind turbine components. Engineering Failure Analysis, 18(1):12–24, 2011.

[55]. Vilaro T, Colin C, and Bartout J. As-fabricated and heat-treated microstructures of the Ti-6Al-4V alloy processed by selective laser melting. Metallurgical and Materials Transactions A, 42(10): 3190–3199, 2011.

[56]. Friedman JH and Stuetzle W. The in-out method for linear regression with censored data. Technical report, Stanford University Technical Report, 1981.

[57]. Guo R, Xu L, Wu J, Yang R, and Zong BY. Microstructural evolution and mechanical properties of powder metallurgy Ti-6Al-4V alloy based on heat response. Materials Science and Engineering: A, 639:327–334, 2015.

[58]. Xu L, Guo R, Bai C, Lei J, and Yang R. Effect of hot isostatic pressing conditions and cooling rate on microstructure and properties of Ti-6Al-4V alloy from atomized powder. Journal of Materials Science & Technology, 30(12):1289–1295, 2014.

[59]. Zhang K, Mei J, Wain N, and Wu X. Effect of hot-isostatic-pressing parameters on the microstructure and properties of powder Ti-6Al-4V hot-isostatically-pressed samples. Metallurgical and Materials Transactions A, 41(4):1033–1045, 2010.

[60]. Cai C, Song B, Xue P, Wei Q, Wu J, Li W, and Shi Y. Effect of hot isostatic pressing procedure on performance of Ti6Al4V: surface qualities, microstructure and mechanical properties. Journal of Alloys and Compounds, 686:55–63, 2016.

[61]. Shirai Y. Inagaki I. Cho K. Niinomi M. Effects of hot working conditions on fatigue strength of Ti-6Al-4V alloy; In Proceedings of the 13th World Conference on Titanium; 811–815.

[62]. Chen W, Boehlert CJ, Payzant EA, and Howe JY. The effect of processing on the 455 °C tensile and fatigue behavior of boron-modified Ti-6Al-4V. International Journal of Fatigue, 32(3):627–638, 2010.

[63]. Seetharaman V.Semiatin SL and Weiss I. Flow behavior and globularization kinetics during hot working of Ti-6Al-4V with a colony alpha microstructure. Materials Science and Engineering: A, 263(2):257–271, 1999.

[64]. Perumal B, Rist MA, Gungor S, Brooks JW, and Fitzpatrick ME. The effect of hot deformation parameters on microstructure evolution of the α-phase in Ti-6Al-4V. Metallurgical and Materials Transactions A, 47(8):4128–4136, 2016.

[65]. Wilkinson DS and Ashby MF. Pressure sintering by power law creep. Acta Metallurgica, 23(11): 1277–1285, 1975.

[66]. Lee BJ and Mear ME. Studies of the growth and collapse of voids in viscous solids. Journal of engineering materials and technology, 116(3):348–358, 1994.

[67]. Helle AS, E Easterling K, and Ashby MF. Hot isostatic pressing diagrams: new developments. Acta Metallurgica, 33(12):2163–2174, 1985.

[68]. Seshacharyulu T, Medeiros SC, Frazier WG, and Prasad YVRK. Microstructural mechanisms during hot working of commercial grade Ti-6Al-4V with lamellar starting structure. Materials Science and Engineering: A, 325(1):112–125, 2002.

[69]. Seshacharyulu T.l., Medeiros SC, Frazier WG, and Prasad YVRK. Hot working of commercial Ti-6Al-4V with an equiaxed α–β microstructure: materials modeling considerations. Materials Science and Engineering: A, 284(1):184–194, 2000.

[70]. Zhang ZX, Qu SJ, Feng AH, Shen J, and Chen DL. Hot deformation behavior of Ti-6Al-4V alloy: Effect of initial microstructure. Journal of Alloys and Compounds, 718:170–181, 2017.

[71]. Luo J, Li M, Yu W, and Li H. The variation of strain rate sensitivity exponent and strain hardening exponent in isothermal compression of Ti-6Al-4V alloy. Materials and Design, 31(2): 741–748, 2010.

- Analysis of literature data provides insight into the mechanism by which HIP treatment improves fatigue life
- We find that HIP improves fatigue life of Ti64 by (1) decreasing the fraction of the defect population that can initiate fatigue cracks, (2) decreasing defect sizes below a threshold, and (3) by changing the microstructure that surrounds defects.
- The idea that microstructure near defects evolves differently than the microstructure away from defects during HIP treatment of Ti64 is supported by EBSD orientation maps.
- The gained understanding is used to provide initial guidance on the HIP soak parameters (Temperature-Pressure-Time) required for improving high cycle fatigue performance in PBF Ti-6Al-4V.

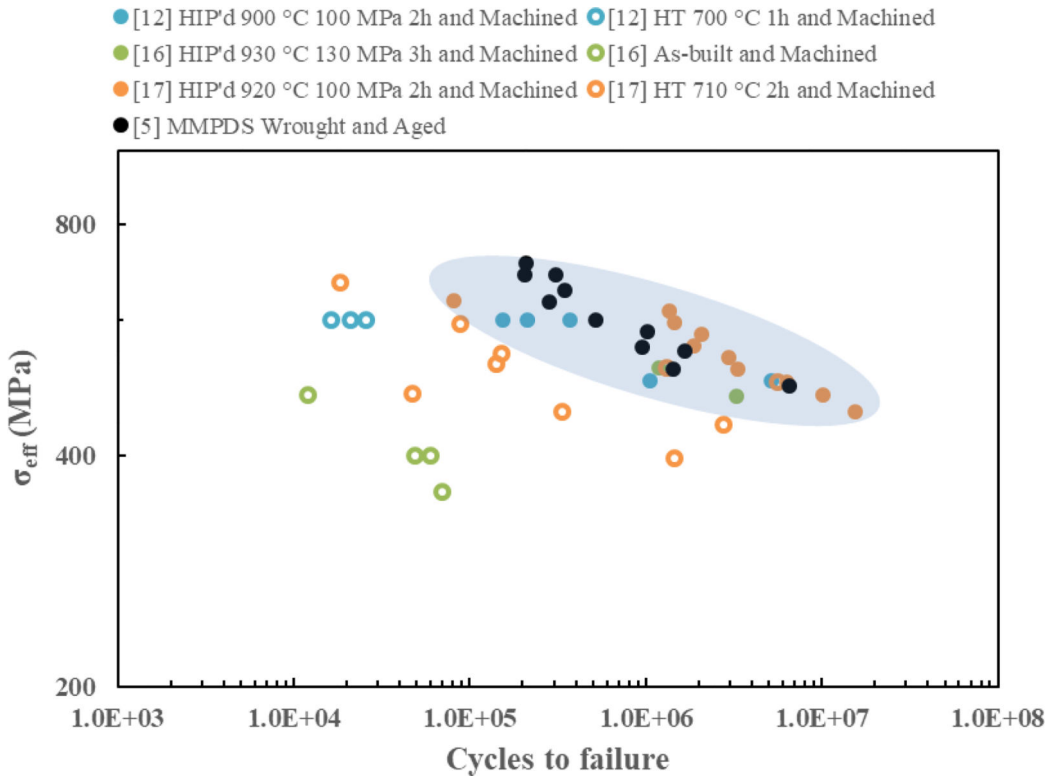

Figure 1:

High cycle fatigue performance of HIP treated laser PBF Ti-6Al-4V reported from 3 independent research groups ([12, 16, 17]) and MMPDS wrought and aged Ti-6Al-4V [5]. To allow for comparison, the fatigue performance is characterized by the expected life at σ_{eff} = 600 MPa, via linearly fitting the published S-N data in a $\log_{10}$-$\log_{10}$ space and using Walker's method [18] to normalize differences in stress ratio, $\sigma_{\text{eff}} = \sigma_{\max}\left(\frac{1-R}{2}\right)^{0.28}$. HT represents heat treated. The gray shaded area highlights the HIP'd and surface machined data.

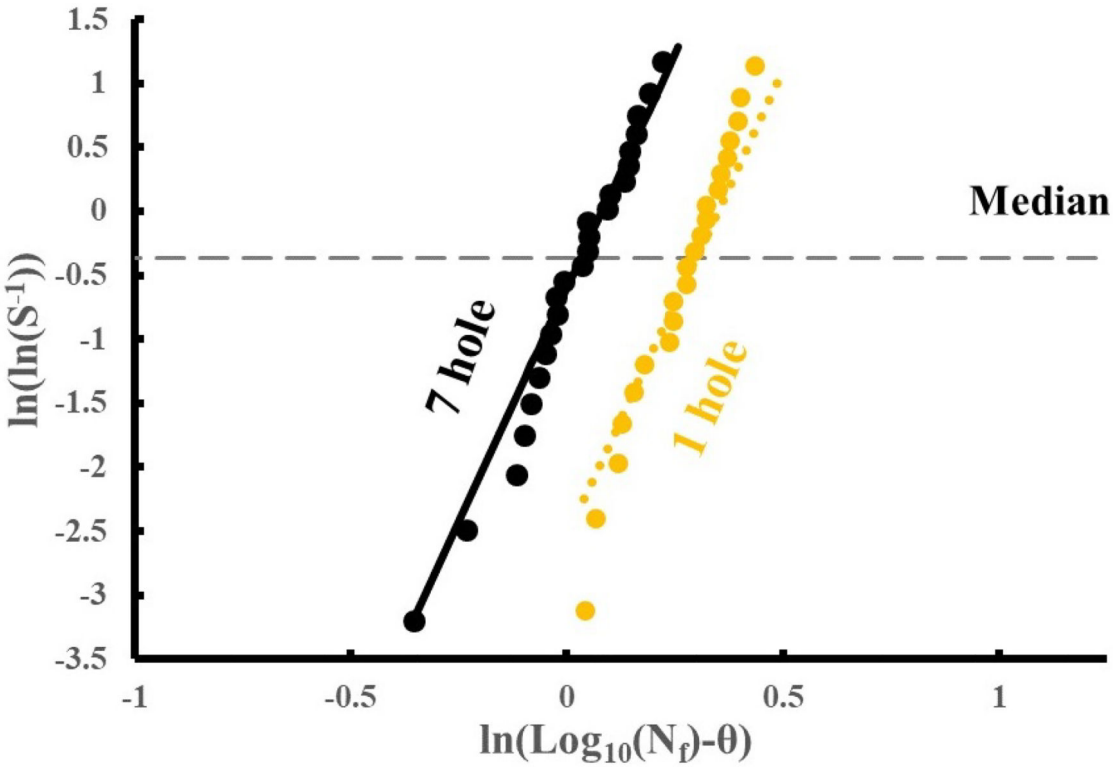

Figure 2:

Weakest link model applied to high cycle fatigue data of Schweiger and Heckel [52]. Sets of otherwise identical specimens had either a single or seven drilled holes. The lines represent model fits. The quality of the fits suggest the ability of the weakest link model to capture the effects of different defect populations.

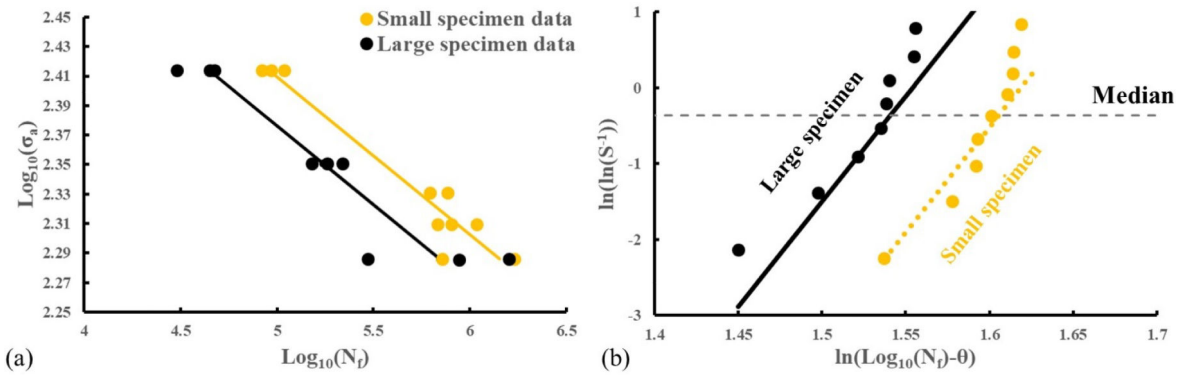

Figure 3:

(a): Shirani and Härkegård's [54] high cycle fatigue data and linear S-N fit for two sets of specimens differing only in size. (b): Weakest link model applied to Shirani and Härkegård's data using the fits shown in (a). The lines represent model fits. The quality of the fits in (b) suggest the extent to which the weakest link model can capture the effect of differences in defect populations on S-N data.

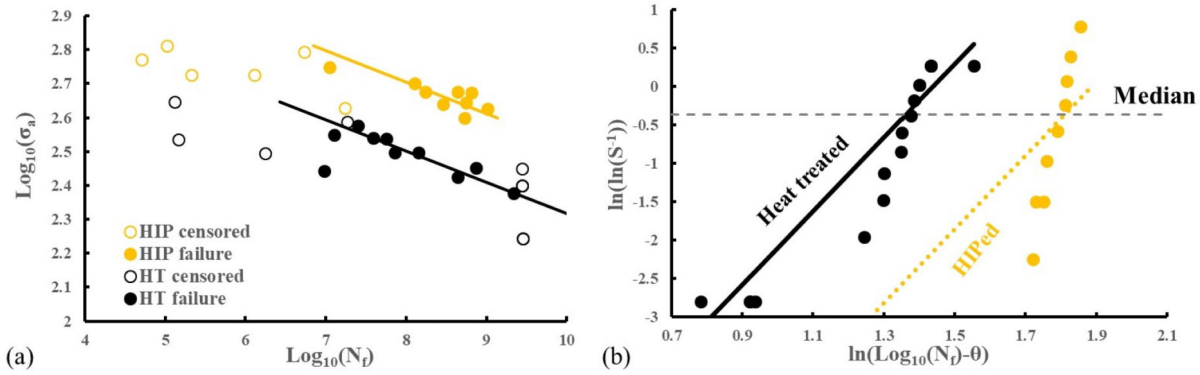

Figure 4:

(a): Günther et al.'s [19] high cycle fatigue data and linear S-N fit for two sets of specimens, HIP'd and heat treated. Censored data is represented by hollow symbols, and was classified as such either due to lack of failure during test or failure via a surface initiated crack. (b): Weakest link model applied to Günther et al.'s data using the fits shown in (a). The lines represent model fits. The lack-of-fit is taken to suggest that the benefits of HIP treatment cannot be explained by a weakest link model considering the impact of HIP treatment on the defect population.

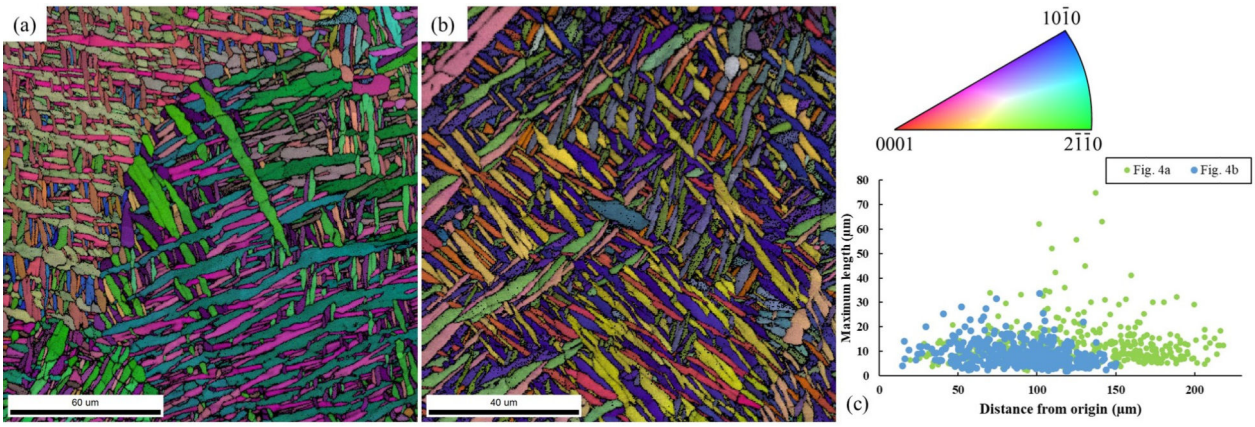

Figure 5:

(a & b) EBSD α phase orientation maps at two locations away from defects and specimen surfaces in HIP treated laser PBF Ti-6Al-4V. EBSD maps were collected by cross-sectioning the specimen perpendicular to the build direction (and specimen loading axis). Crystal orientations in the inverse pole figure (IPF) map are normal to the cross section. (c) Scatter plot showing the maximum length of α grains in the scanned plane as a function of the distance to the origin of the image (bottom left corner). The x-axis was chosen to enable direct comparison with Fig. 6d.

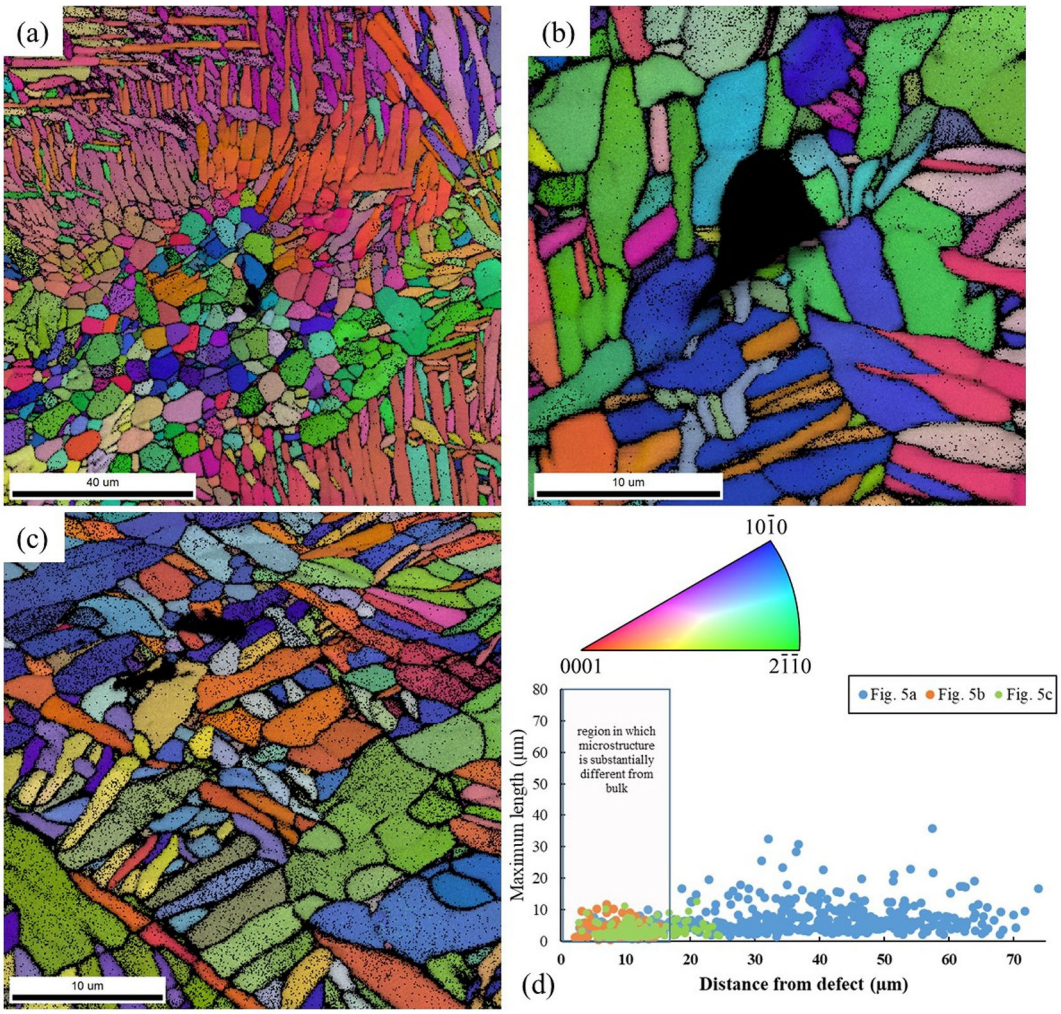

Figure 6:

(a, b & c) EBSD α phase orientation maps near defects in HIP treated laser PBF Ti-6Al-4V. EBSD maps were collected by cross-sectioning the specimen perpendicular to the build direction (and specimen loading axis). Crystal orientations in the IPF map are normal to the cross section. (d) Scatter plot showing the maximum length of α grains in the scanned plane as a function of the distance to the center of the defect (where in (c) only the top right pore was analyzed.)

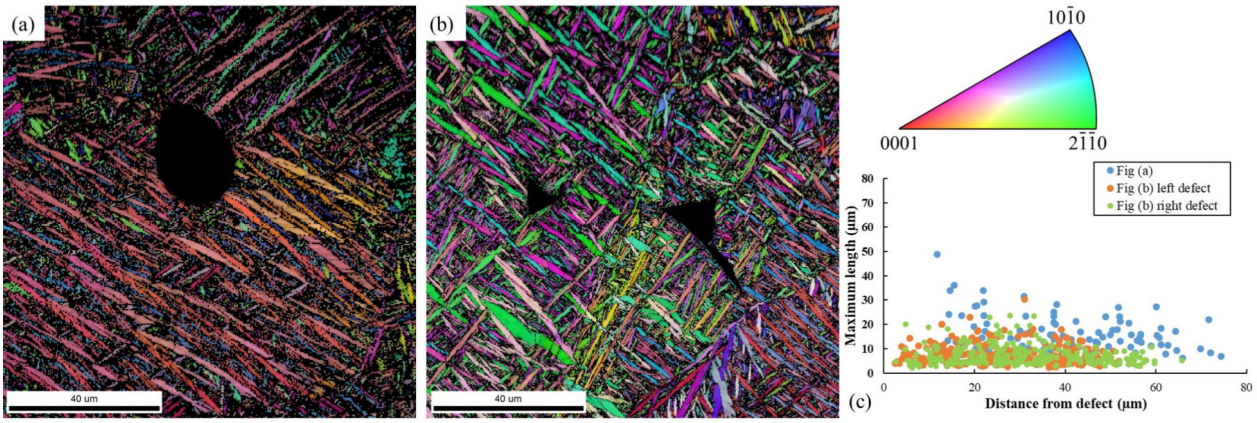

Figure 7:

(a & b) EBSD α phase orientation maps around three defects in laser PBF Ti-6Al-4V prior to HIP treatment. EBSD maps were collected by cross-sectioning the specimen perpendicular to the build direction (and specimen loading axis). Crystal orientations in the IPF map are normal to the cross section. (c) Scatter plot showing the maximum length of α grains in the scanned plane as a function of the distance to the center of the defect. The images and the scatter plot do not show a distinct difference in the microstructure near defects than that away from defects in contrast to the HIP treated material.

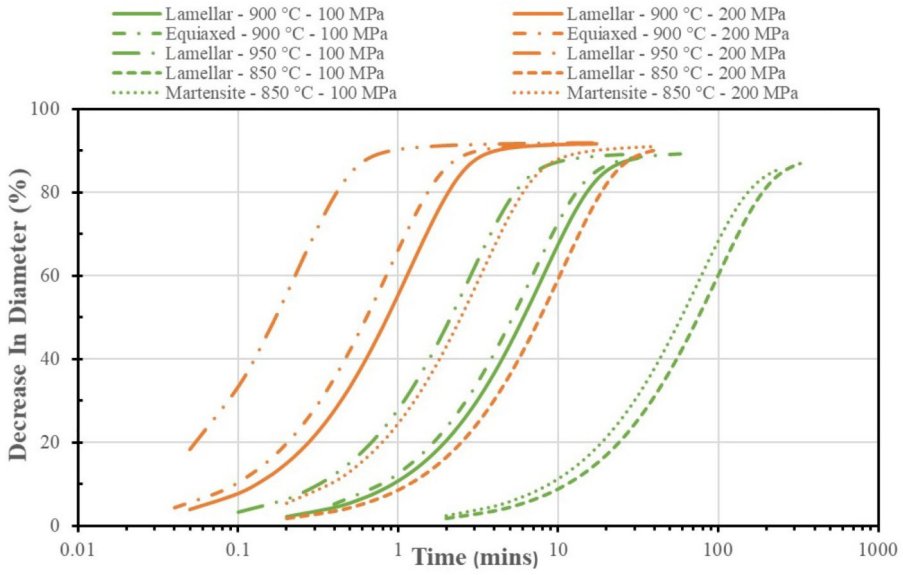

Figure 8:

The predicted diameter evolution of spherical argon filled pore type defects using material constants from Table 1. Cases of starting lamellar [69], equiaxed [68] and martensitic [70] microstructures with HIP pressures of 100 and 200 MPa, and HIP temperatures of around 900 °C are shown here for reference.

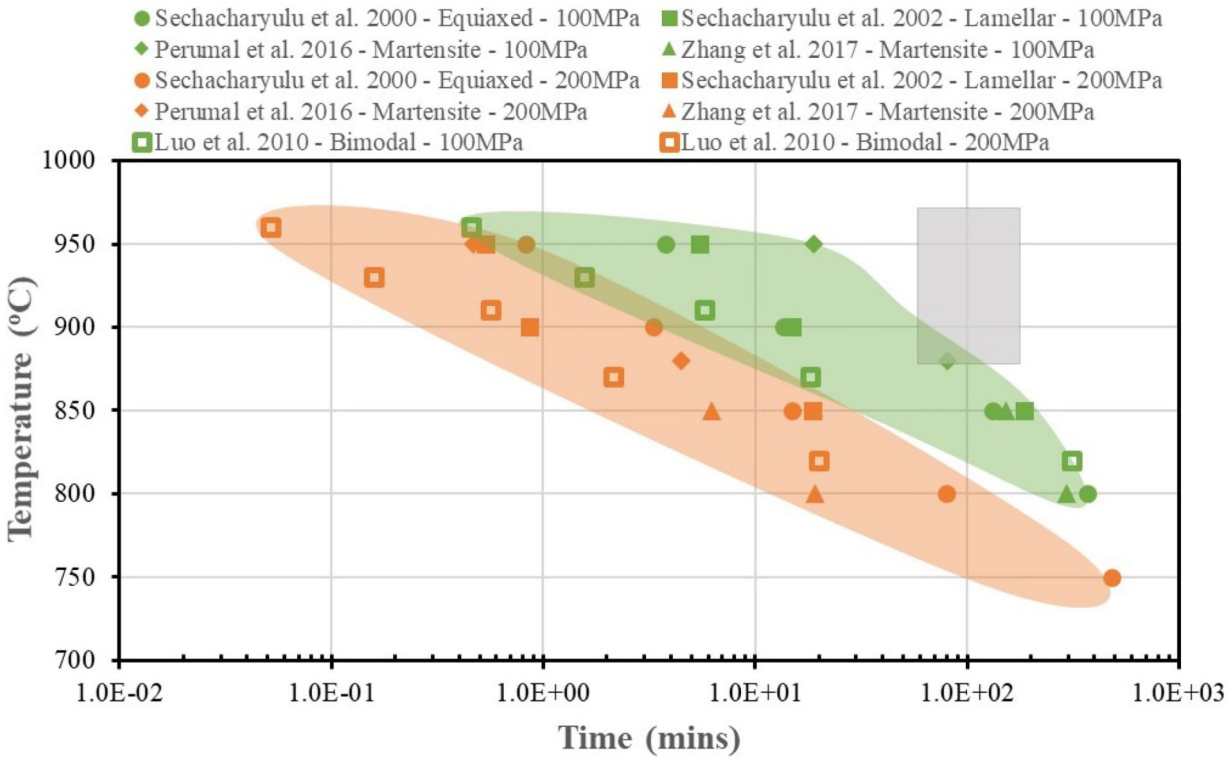

Figure 9:

Predicted temperature-time map of HIP soak conditions required to decrease defect diameters by at least 80 %. The colored regions encapsulate predictions made with the same HIP pressure but different material properties resulting from different starting microstructures and data collection procedures. Based on current understanding, times and temperatures above the colored regions are likely to neutralize fatigue initiating defects in the bulk. The gray block represents the standard HIP practices commonly used [3].

Table 1:

Parameter constants used for Wilkinson-Ashby's model fit from experimental data of the as-cast/as-received Ti-6Al-4V bars during hot working.

Source	A	n	Temperature (°C)	Starting Microstructure
Sechacharyulu et al. 2002 [68]	1.374E-16	5.817	750	Lamellar
	3.561E-14	5.084	800	
	1.142E-09	3.265	850	
	5.787E-08	2.775	900	
	3.762E-11	3.279	950	
Sechacharyulu et al. 2000 [69]	5.112E-11	3.477	750	Equiaxed
	4.723E-10	3.338	800	
	9.734E-10	3.444	850	
	9.734E-08	3.053	900	
	5.523E-09	4.132	950	
Perumal et al. 2016 [64]	3.146E-10	4.054	880	Martensitic
	9.414E-11	5.144	950	
Zhang et al. 2017 [70]	1.342E-10	3.882	800	Martensitic
	5.333E-11	4.505	850	
Luo et al. 2010 [71]	1.253E-10	3.887	820	Bimodal
	2.387E-08	3.011	870	
	3.053E-08	3.322	910	
	1.949E-07	3.137	930	
	8.417E-07	4.054	960	